DOI: 10.1002/adma.200702554

Control of Electric Field Strength and Orientation at the Donor–Acceptor Interface in Organic Solar Cells**

By *Albert Liu*, *Shanbin Zhao*, *Seung-Bum Rim*, *Junbo Wu*, *Martin Könemann*, *Peter Erk*, and *Peter Peumans**

Organic solar cells have attracted research interest due to the promise of low-cost manufacturing on flexible substrates. Since the introduction of efficient donor-acceptor heterostructures by Tang,[1] the power conversion efficiency (PCE) of organic solar cells has steadily increased from 0.95 % under 1 sun AM 1.5G illumination to present values of ca. 6 % for both small molecule and polymer devices.[2,3] While recent progress in raising the power conversion efficiency has been encouraging, these values are still well below efficiencies required for commercial applications. Further improvements in both material properties and device architectures are necessary.

Photocurrent generation in an organic solar cell is fundamentally different from the process that takes place in their inorganic counterparts because the absorption of light leads to bound electron–hole pairs, known as excitons, with binding energies ranging from 0.1–2 eV.[4–6] Because the built-in electric fields in organic solar cells is limited, exciton dissociation in the absence of a DA interface is inefficient.[7] Efficient dissociation of the strongly bound excitons requires either a stronger electric field ($F > 10^6$ V cm^{-1}) or a donor-acceptor (DA) heterojunction, where the difference between the electron affinities and ionization potentials of the donor and acceptor material lead to fast charge transfer across the interface.[8] This results in a geminate electron–hole pair (GEHP) that is still bound by a Coulomb force, with the electron in the acceptor lowest unoccupied molecular orbital (LUMO) and the hole in the donor highest occupied molecular orbital (HOMO). Dissociation of the GEHP and collection of the electron and hole at their respective electrodes leads to photocurrent.

Most models of organic solar cell operation assume a metal-insulator-metal (MIM) model, where the built-in electric field is established by the work function difference between the anode and cathode.[5] The MIM model assumes negligible doping in the active organic layers and predicts a uniform electric field, F, throughout the device thickness in the absence of space charge, leading to the energy level diagram of Figure 1a. This model is problematic because the maximum achievable built-in electric field, F, at the DA interface is:

$$F = (HOMO_D - LUMO_A - \Delta E)/qd, \quad (1)$$

where $HOMO_D$ is the donor HOMO, $LUMO_A$ is the acceptor LUMO, ΔE is sum of the difference between cathode Fermi level and acceptor LUMO and anode Fermi level and donor HOMO, q is the elementary charge and d is the device active

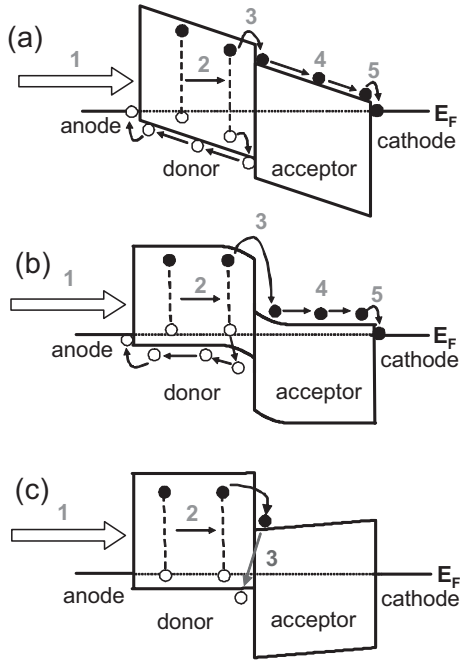

Figure 1. a) Energy level diagram for the conventional metal-insulator-metal (MIM) model of an organic DA solar cell at 0 V. The five steps of photocurrent generation described in the text are illustrated. b) Energy level diagram of a DA solar cell at 0 V with a p-type doped donor and n-type doped acceptor. The donor and acceptor layers are 30 nm thick and have a doping concentration of 10^{18} cm^{-3}. c) Energy level diagram of DA solar cell at 0 V for the case of a donor p-type doping of 10^{17}cm^{-3} and acceptor n-type doping of 10^7 cm^{-3}.

[*] Prof. P. Peumans, S.-B. Rim
Electrical Engineering Department, Stanford University
Stanford, CA 94305 (USA)
E-mail: ppeumans@stanford.edu
A. Liu, S. Zhao, J. Wu
Materials Science and Engineering Department, Stanford University
Stanford, CA 94305 (USA)
M. Könemann, P. Erk
BASF GmbH
Ludwigshafen 67056 (Germany)

[**] This work was supported by BASF AG. The authors would like to thank W. Jaegermann for UPS data on BPE-PTCDI.

ADVANCED MATERIALS

layer thickness. For many DA systems,[1,9] $HOMO_D - LUMO_A$ = 0.7–1.0 eV, ΔE = 0.3eV,[10] and a typical active layer thickness is d = 100 nm, resulting in $F < 0.8 \times 10^5$ V cm^{-1}. According to an earlier analysis,[7] GEHPs are not dissociated efficiently until F significantly exceeds 10^5 V cm^{-1}.

In this Communication, we show that in many small molecular weight organic DA solar cells, unintentional electrical doping is present and has a dominant effect on the built-in electric field at the DA interface, and consequently, on the efficiency with which GEHPs are dissociated and on the overall power conversion efficiency. An energy level diagram similar to that of Figure 1b would be obtained if the acceptor and donor were n-type and p-type doped, respectively, leading to a concentration of the built-in potential drop at the DA interface and strong electric fields that assist the GEHP separation. The potential drop is no longer dominated by the alignment of the electrode Fermi levels within the organic semiconductor bandgap, but is determined by the position of the Fermi level in the donor and acceptor layer which is a function of the electrically active doping concentration. If the doping is absent or of the wrong type, as shown in Figure 1c, the electric field at the DA interface prevents the GEHP from separating, leading to low efficiencies.

The donor material copper phthalocyanine (CuPc) was used throughout this work. The acceptor materials used are *N*,*N*'-bis(2-phenylethyl)-perylene-3,4,9,10-tetracarbonicacid-diimide (BPE-PTCDI, molecular structure in the inset of Fig. 2a) and *N*,*N*'-diphenyl-perylene-3,4;9,10-tetracarbonicacid-diimide (DP-PTCDI) (both supplied by BASF), as well as C_{60} (purchased from MER Corporation).[9] Recent studies have shown BPE-PTCDI to be an excellent n-channel organic semiconductor, possessing both a high n-type mobility (≈ 0.1 cm^2 V^{-1} s^{-1}) and good stability in air over several weeks.[11] A remarkably long exciton diffusion length of 2.3 μm was estimated[12] for solvent-annealed, evaporated thin films of this material, making it an attractive candidate for use in bilayer device structures. Its HOMO level was measured to be –6.1 eV by ultraviolet photoelectron spectroscopy (IPES)[13] indicating that it is a strong acceptor with respect to CuPc (HOMO = –5.0 eV).[14] All materials were purified by gradient sublimation unless noted otherwise.

BPE-PTCDI was purified by three consecutive gradient sublimations. Purified and as-synthesized (i.e., impure) BPE-PTCDI were used to fabricate CuPc/BPE-PTCDI solar cells. Matrix-assisted laser desorption/ionization (MALDI) was performed on both the purified and impure materials to determine the effectiveness of thermal gradient purification. As shown in Figure 2a, the MALDI spectrum of the purified material is dominated by a set of peaks at a molecular weight MW = 598, corresponding to BPE-PTCDI. The impure material, on the other hand, contains significant amounts of various additional compounds. While the thin film deposition process itself introduces a small degree of additional purification not reflected in the MALDI data, special care was taken to refill the evaporation sources with as-synthesized BPE-PTCDI after each deposition ($\approx$ 2 min) to ensure reproducible

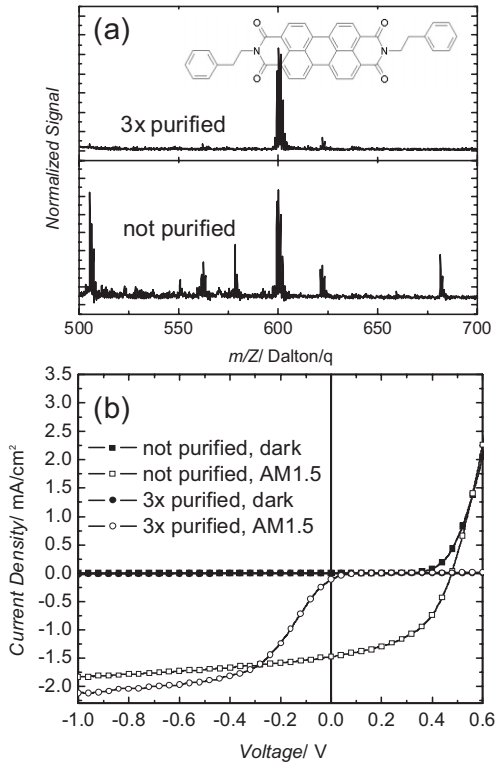

Figure 2. a) MALDI spectra of unpurified (bottom) and 3 × purified (top) BPE-PTCDI (MW = 598). A large fraction of impurities is removed after thermal gradient purification. Inset: Chemical structure of BPE-PTCDI. b) Current density–voltage (J–V) curves for identical device structures (ITO/34 nm CuPc/34 nm BPE-PTCDI/100 nm Ag) with purified (circles) and impure (squares) BPE-PTCDI in the dark (filled symbols) and under (88 ± 4) mW cm^{-2} AM1.5G illumination (open symbols).

data for unpurified BPE-PTCDI devices. Since it has been shown that organic solar cell performance is sensitive to the impurity content in the active layers, with device performance increasing 2–4 times depending on the number of gradient purification cycles,[15,16] the performance of devices with purified BPE-PTCDI is expected to be superior over that of devices made using the impure compound.

The current density-voltage (J–V) curves for identical device structures (ITO/34 nm CuPc/34 nm BPE-PTCDI/100 nm Ag) with purified (circles) and impure (squares) BPE-PTCDI in the dark (filled symbols) and under (88 ± 4) mW cm^{-2} AM1.5G illumination (open symbols), are shown in Figure 2b. The power conversion efficiency of the device using impure BPE-PTCDI is η = 0.39 % versus η = 0.002 % for a device that uses purified BPE-PTCDI. The devices that use impure BPE-PTCDI outperform devices that use the pure compound in open circuit voltage (V_{OC}), short-circuit current density (J_{SC}), and fill-factor (FF). The characteristics of the device made with impure BPE-PTCDI that was exposed to air for 4 h fall in between those of a device with pure BPE-PTCDI and impure BPE-PTCDI (discussed in Fig. 4). The photocurrent density (i.e., the difference between the J–V curves under illumination and in the dark) versus voltage characteristics of the device

using purified BPE-PTCDI is approximately that of the device based on the impure compound shifted by 0.55 V toward negative voltages, suggesting that the difference between these devices is due to a difference in built-in potential.

To investigate the origins of the large difference in *J–V* characteristics, capacitance–voltage (*C–V*) measurements were carried out at a frequency of 10 kHz to determine the electrical doping concentrations in the organic active layers. In Figure 3a, the *C–V* characteristics of devices using impure BPE-PTCDI (squares), impure BPE-PTCDI after 4 h exposure to air (circles) and 3× purified BPE PTCDI (triangles), are shown. The device based on impure BPE-PTCDI exhibits

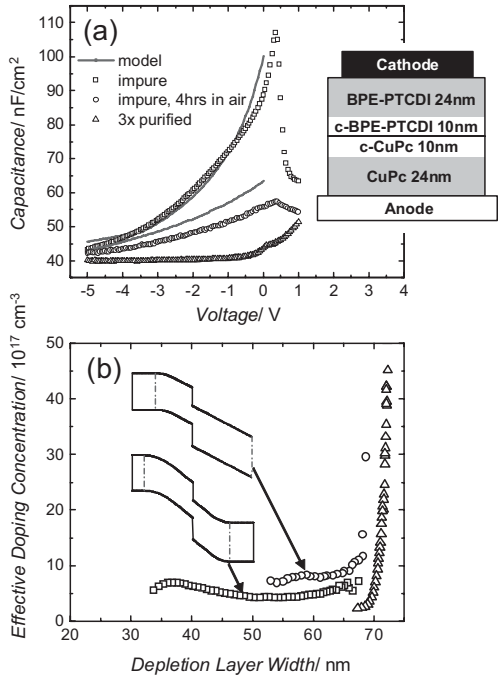

Figure 3. a) Capacitance-voltage (*C–V*) characteristics of devices using impure BPE-PTCDI (squares), impure BPE-PTCDI after 4 h exposure to air (circles) and 3x purified BPE-PTCDI (triangles). Fitted model data (see text) is shown as a solid line. Inset: Schematic of the device structure used to model *C–V* and *J–V* data. b) Effective doping concentration vs. depletion layer width extracted from *C–V* data shown in (a). Top inset: Calculated energy level diagram of the partially de-doped (4 h air exposure) device at –2 V. The BPE-PTCDI layer is completely depleted. Bottom inset: Calculated energy level diagram of the doped (fresh device based on impure BPE-PTCDI) device at –2 V.

a strong voltage-dependence of its capacitance akin to a conventional pn-junction indicating the presence of a depletion layer. The capacitance of the device based on purified BPE-PTCDI, on the other hand, is pinned at the geometric capacitance indicating that the device is completely depleted. The *C–V* of the device based on impure BPE-PTCDI that was exposed to air for 4 h falls in between the above two extremes.

The spatial profile of the doping concentration was extracted using:[17]

$$N_B(W) = \frac{2}{qK_s\varepsilon_0 A^2 \left| d\left(1/C^2\right)/dV_A \right|}, \quad (2)$$

where $W = K_S\varepsilon_0 A/C$ and $N_B = N_A N_D/(N_A + N_D)$, K_S is the dielectric constant, ε_0 is the permittivity of free space, A is the area of the capacitor, N_A is the p-type doping concentration in the donor layer and N_D is the n-type doping concentration in the acceptor layer, both evaluated at the edge of the depletion region. This expression is evaluated as a function of voltage, V, which determines the depletion layer width, W. Measurements of doping using *C–V* profiling only determine the effective doping concentration, N_B, which is dominated by the layer with the lowest doping concentration (i.e., if $N_A >> N_D$, $N_B \cong N_D$). If one layer of the donor/acceptor couple is completely depleted, the depletion region extends into the electrode in contact with the depleted layer such that:

$$N_B = \frac{N_{\text{electrode}}\, N_{\text{undepleted}}}{N_{\text{electrode}} + N_{\text{undepleted}}}, \quad (3)$$

where $N_{\text{electrode}}$ is the charge density of the electrode in contact with the completely depleted layer and $N_{\text{undepleted}}$ is the doping concentration of the remaining undepleted organic layer. Since $N_{\text{electrode}} >> N_{\text{undepleted}}$, N_B is an accurate indicator of the actual doping concentration in the remaining undepleted organic layer.

A plot of N_B versus W is shown in Figure 3b. The devices that use impure BPE-PTCDI (squares) have a minimum depletion layer width of 32 nm and $N_B = (6 \pm 2) \times 10^{17}$ cm^{-3}. The impurities responsible for the n-type doping of BPE-PTCDI are presently unknown. After exposure to air for 4 h (circles), the n-doping concentration of BPE-PTCDI appears to be reduced, as monitored by a decrease in maximum capacitance or increase in the minimum depletion layer width. As the BPE-PTCDI layer becomes de-doped and depleted of free charge carriers, the effective doping concentration, N_B, as determined via *C–V* measurements, is the activated p-type doping concentration in the remaining undepleted CuPc layer: $N_B = N_A = (7.5 \pm 1.5) \times 10^{17}$ cm^{-3} (Fig. 3b, inset), in agreement with prior observations.[18] The minimum depletion layer width increases from 32 nm for an as-fabricated device with impure BPE-PTCDI to 50 nm after 4 h in air and 60 nm (nearly complete depletion) after 24 h in air (not shown). The *C–V* characteristics of a device based on purified BPE-PTCDI (triangles) is identical to that of one based on the impure compound exposed to air for 24 h. Based on the above estimate of the p-type doping concentration in CuPc, the n-type doping concentration in BPE-PTCDI was estimated by fitting the *C–V* experimental data to a simple model (Fig. 3a, solid lines). The model device structure is: 24 nm doped CuPc/10 nm compensated CuPc/10 nm compensated BPE-PTCDI/24 nm doped BPE-PTCDI (Fig. 3a, inset). The 20 nm thick compensated region has previously been observed in CuPc/PTCBI devices.[18] In the model calculations, we used the HOMO levels of CuPc (–5.0 eV)[14] and BPE-PTCDI (–6.1 eV)[13] obtained via ultraviolet photoelectron spectroscopy measurements. The LUMO levels were determined to be –3.2eV for CuPc and –4.1 eV for BPE-PTCDI based on IPES.[13] An effective density states of 10^{21} cm^{-3} at the molecular transport

ADVANCED MATERIALS

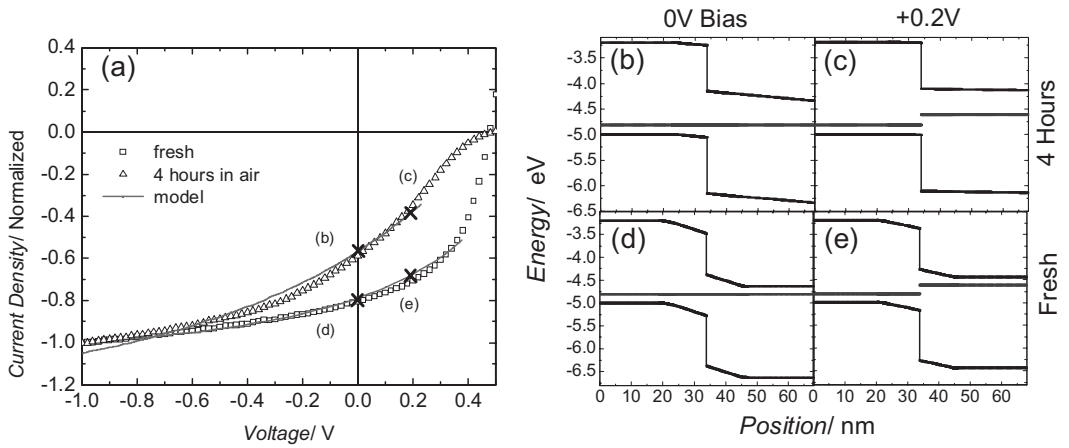

Figure 4. a) *J–V* curves of ITO/CuPc (34 nm)/unpurified BPE-PTCDI (34 nm) devices with minimal (open squares) and 4hrs (open triangles) of air exposure. Kinetic Monte Carlo simulation results (see text) are also shown (solid lines). b)–e) Calculated energy level diagrams corresponding to the x-markers in (a) and doping concentrations estimated from the models of Figure 3a.

levels is assumed, in line with previous calculations of Fermi levels in disordered organic solids.[7,19] Using these parameters, n-type doping concentrations of $(1.2 \pm 0.5) \times 10^{18}$ cm^{-3} and $1 \times 10^{13 \pm 1}$ cm^{-3} are obtained for fresh devices and devices exposed to air for 4 hours, respectively.

Similar unintentional electrical doping is observed in other efficient cells even if the materials were purified by repeated gradient sublimation. The effective doping in ITO/CuPc/3,4,9,10 perylenetetracarboxylic bisbenzimidazole (PTCBI)/Ag cells was reported to be $N_B = (8 \pm 2) \times 10^{17}$ cm^{-3}.[18] We determined the average effective doping of a ITO/CuPc/C60/Ag device[9] to be $N_B = (1.5 \pm 0.5) \times 10^{17}$ cm^{-3}. In both the PTCBI and C_{60} cases, purification by multiple gradient sublimation runs did not remove the n-type doping of the acceptor. The ability to remove the n-type dopant in BPE-PTCDI by gradient sublimation appears to be a less common situation that permits the evaluation of the effect of electrical doping.

Previous explanations for improved solar cell performance upon doping the organic layers attributed the effects to an increased conductivity of the organic layers[20] and removal of Schottky barriers at the organic/metal interface.[21] The high resistivity hypothesis prior to doping is inconsistent with the photocurrent curve of the undoped device being a translated version of that of the doped device. Schottky barriers play a minor role since previous studies have shown that varying the cathode material workfunction does not prevent efficient carrier extraction, despite forming non-ohmic contacts in many cases.[22]

Our observations and those of other groups can be explained on the basis of the orientation and magnitude of the electric field at the DA junction that is responsible for GEHP separation. In Figure 4b–d, energy level diagrams at 0 V and +0.2 V, computed based on the doping profiles extracted from C-V measurements, are shown for devices with impure (i.e., doped) BPE-PTCDI and devices that are partially de-doped by exposure to air. The *I–V* curves are also shown for reference in Figure 4a (doped: squares, partially de-doped: triangles). In the case of the impure BPE-PTCDI, the electric field at the DA interface ($F = 2.2 \times 10^5$ V cm^{-1} at 0 V and $F = 1.5 \times 10^5$ V cm^{-1} at +0.2 V) is able to efficiently dissociate GEHPs, even at 0.2 V forward bias. In contrast, when the doping is partially removed by air exposure, the electric field weakens considerably ($F = 5.3 \times 10^4$ V cm^{-1} at 0 V and $F = 8.6 \times 10^3$ V cm^{-1} at +0.2 V), making GEHP separation less likely and reducing the quantum efficiency and photocurrent. We have previously reported on kinetic Monte Carlo calculations of the dependence of the GEHP separation probability on applied bias at a DA interface.[7] Identical calculations were performed by calculating the electric field profiles as a function of applied bias, for the devices of Figure 4. The parameters used for these calculations are: 2 nm initial separation of the electron–hole pairs at the DA interface, identical hopping rates for electrons and holes, and a recombination rate for adjacent electrons and holes that is 1/10th the charge hopping rate. The calculations of GEHP separation probability were performed from –1 V negative bias to flatband conditions, and the calculated probability was subsequently multiplied by a scaling factor to fit the experimental photocurrent data.[7] The experimental J-V curves were normalized to the same value at –1 V negative to allow a side-by-side comparison of their dependence on applied bias. The resulting dependence of the GEHP separation probability fits the dependence of photocurrent, as shown in Figure 4 (solid lines), supporting the hypothesis that changes in the electric field at the DA interface are responsible for a the change in the *I–V* characteristics and solar cell efficiencies through their influence on the GEHP separation probability.

To further confirm that electrical doping is responsible for the observations, the n-type dopant Pyronin B chloride was introduced into devices with purified BPE-PTCDI. Pyronin B chloride is a cationic dye that was previously used to n-type dope a variety of electron transport materials.[23,24] The dopant and host material were deposited by co-evaporation into the following structure: ITO/34 nm CuPc/34 nm Pyronin

B:BPE-PTCDI/100 nm Ag. The dopant was not purified prior to use. As shown in Figure 5a, intentional n-type doping of BPE-PTCDI with Pyronin B chloride at weight fractions of 1:1 (squares) and 1:35 (circles) improves the *J–V* characteristics of the devices with respect to the device with undoped

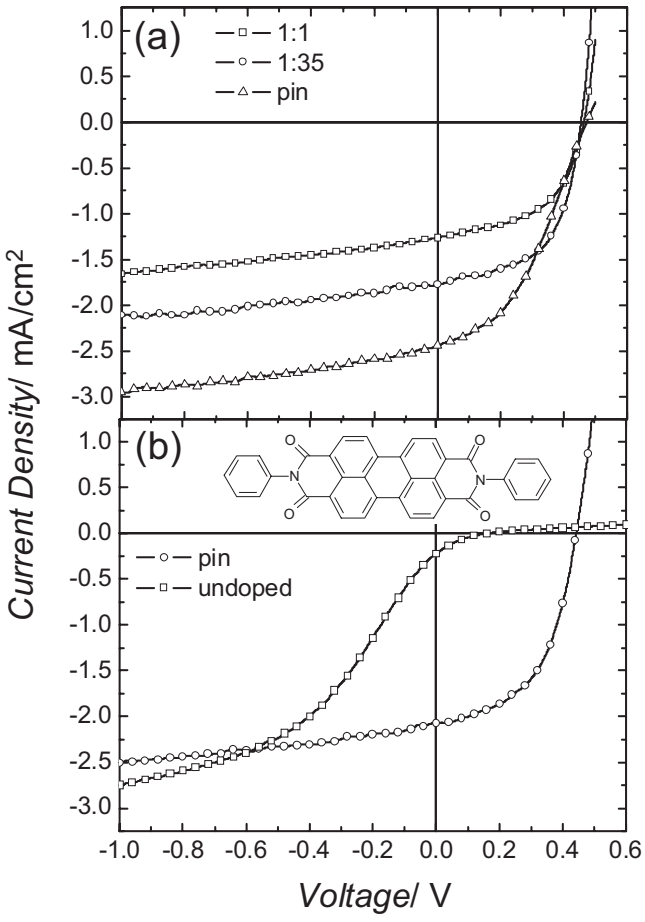

Figure 5. a) Comparison of *J–V* curves of ITO/34 nm CuPc/34 nm BPE-PTCDI/100 nm Ag with different weight fractions of Pyronin B chloride in purified BPE-PTCDI under (88± 4) mW cm^{-2} AM1.5G illumination. The Pyronin B chloride weight fractions shown are 1:1 (open squares) and 1:35 (open circles). The *J–V* characteristics of a p-i-n device structure (open triangles) ITO/34 nm CuPc/11 nm undoped BPE-PTCDI/23 nm 1:25 Pyronin B chloride:BPE-PTCDI/100 nm Ag. The lines are a guide to the eye. b) *J–V* characteristics of ITO/34 nm CuPc /34 nm DP-PTCDI/100 nm Ag devices (open squares) and ITO/34 nm CuPc/11 nm DP-PTCDI/23 nm 1:40 Pyronin B chloride:DP-PTCDI/100 nm Ag devices (open circles) under (88 ± 4) mW cm^{-2} AM1.5G illumination. The lines are a guide to the eye. Inset: Chemical structure of DP-PTCDI.

BPE-PTCDI (Fig. 2b, circles), confirming that n-type doping of the acceptor is necessary for efficient GEHP separation. Higher doping concentrations lead to a reduction in J_{SC}, presumably because the presence of the dopant inhibits exciton transport. A further increase in J_{SC} is obtained for a p-i-n device structures of the layer structure ITO/34 nm CuPc/23 nm BPE-PTCDI/11 nm 1:25 Pyronin B:BPE-PTCDI/100 nm Ag (triangles), in agreement with this hypothesis. The p-i-n device structure distributes the built-in voltage drop over a larger spatial range, lowering the electric field at the DA junction and thereby lowering the GEHP separation probability. This is apparent in the *I–V* curves for the p-i-n device structure where the *FF* is ~ 30 % lower than that of the pn device structures.

To show that electrical doping is a general phenomenon, we also show the improvement in device performance in the acceptor material DP-PTCDI (purified by gradient sublimation, molecular structure in the inset of Fig. 5b) upon doping with Pyronin B in Figure 5b. The device structures are: ITO/34 nm CuPc/34 nm DP-PTCDI/100 nm Ag, and ITO/34 nm CuPc/11 nm DP-PTCDI/23 nm 1:40 Pyronin B:DP-PTCDI/100 nm Ag. The n-type doping concentration of the purified DP-PTCDI was too low to create a sufficiently strong field at the DA interface. As this example demonstrates, in the course of testing new solar cell materials it is of crucial importance to determine whether poor device properties are inherent to a material or can be corrected using electrical doping.

We note that electrical doping may be less effective in bulk heterojunction (BHJ) organic solar cells if the depletion layer width (typically ca. 20 nm) is larger than the domain size. This explains why many small molecular weight[25] and all-polymer[26] disordered BHJ solar cells have strongly voltage dependent photocurrents and low efficiencies. Efficient polymer/fullerene[27] and small molecule/C_{60}[28] BHJ solar cells likely employ additional mechanisms to effectively separate GEHPs.

In conclusion, we have shown that providing a strong electric field at the donor-acceptor heterointerface in bilayer DA organic solar cells is essential to the efficient operation of this type of solar cell. This is due to the strong Coulomb attraction between the electron and hole that are generated in close proximity upon exciton dissociation. To limit losses in electrochemical potential associated with this field, it must be concentrated near the DA interface by n- and/or p-doping of the acceptor and donor material, respectively. Many of the most extensively studied and efficient small molecular weight solar cells appear to have unintentional doping of the correct type that is hard to remove.

Experimental

Materials and Sample Preparation: CuPc was obtained from Sigma–Aldrich, BPE-PTCDI and DP-PTCDI were obtained from BASF AG, Pyronin B chloride was obtained from Acros Organics, and C_{60} was obtained from MER Corporation. The materials were purified using two or more consecutive vacuum gradient sublimations. Pyronin B chloride was used as received. During purification, the base pressure was <10^{-6} Torr prior to initial heating of the starting material.

Solar Cell Fabrication: The organic solar cells were fabricated on glass substrates pre-coated with a 140 nm thick ITO anode with a sheet resistance of 12 Ω/square obtained from Optera Colorado, Inc. The substrates were cleaned in acetone, ethanol, and isopropanol followed by a UV-ozone treatment for 15 minutes. The organic layers and silver cathode were deposited by vacuum thermal evaporation in a system with a base pressure below 10^{-6} Torr. For all devices, CuPc was used as the donor material. BPE-PTCDI, DP-PTCDI, and C_{60}

ADVANCED MATERIALS

were independently deposited on CuPc, followed by the deposition of a 100 nm thick Ag cathode through a shadow mask with 0.3 mm diameter openings. For intentionally doped devices, Pyronin B was co-deposited with the acceptor layers. All organic layers were deposited at a rate of 0.1–0.5 nm s^{-1}, and the silver cathode was deposited at a rate of 0.4–0.5 nm s^{-1}.

J–V characteristics at room temperature (25 °C) in the dark and under simulated AM1.5G solar illumination from a filtered 500 W xenon lamp (Sciencetech) were measured using an HP 4145B semiconductor parameter analyzer. The illumination intensity was measured using a calibrated silicon photodiode. *C–V* characteristics were measured using an HP 4192A LF Impedance Analyzer at a frequency of 10 kHz.

Received: October 10, 2007

[1] C. W. Tang, *Appl. Phys. Lett.* **1986**, *48*, 183.
[2] J. G. Xue, S. Uchida, B. P. Rand, S. R. Forrest, *Appl. Phys. Lett.* **2004**, *85*, 5757.
[3] J. Y. Kim, K. Lee, N. E. Coates, D. Moses, T. Nguyen, M. Dante, A. J. Heeger, *Science* **2007**, *317*, 222.
[4] B. A. Gregg, M. C. Hanna, *J. Appl. Phys.* **2003**, *93*, 3605.
[5] H. Hoppe, N. S. Sariciftci, *J. Mater. Res.* **2004**. *19*, 1924.
[6] I. G. Hill, A. Kahn, Z. G. Soos, R. A. Pascal, *Chem. Phys. Lett.* **2000**, *327*, 181.
[7] P. Peumans, S. R. Forrest, *Chem. Phys. Lett.* **2004**. *398*, 27.
[8] N. S. Sariciftci, L. Smilowitz, A. J. Heeger, F. Wudl, *Science* **1992**, *258*, 1474.
[9] P. Peumans, S. R. Forrest, *Appl. Phys. Lett.* **2001**. *79*, 126.
[10] M. C. Scharber, D. Mühlbächer, M. Koppe, P. Denk, C. Waldauf, A. J. Heeger, C. J. Brabec, *Adv. Mater.* **2006**. *18*, 789.
[11] M. M. Ling, P. Erk, M. Gomez, M. Koenemann, J. Locklin, Z. Bao, *Adv. Mater.* **2007**. *19*, 1123.
[12] B. A. Gregg, J. Sprague, M. W. Peterson, *J. Phys. Chem. B* **1997**, *101*, 5362.
[13] Personal communication with W. Jaegermann at Darmstadt University of Technology.
[14] A. Kahn, N. Koch, W. Cao, *J. Polym. Sci. Part B* **2003**, *41*, 2529.
[15] A. Petrich, M. Koch, S. Pfutzner, R. Meerheim, S. Scholz, J. Drechsel, K. Walzer, M. Pfeiffer, K. Leo, *Digest of Technical Papers - SID International Symposium.* (Ed: A.I. Lakatos), Society for Information Display, San Jose, CA **2006**, *37*, 1692.
[16] R. F. Salzman, J. Xue, B. P. Rand, A. Alexander, M. E. Thompson, S. R. Forrest, *Org. Electron.* **2005**, *6*, 242.
[17] S. M. Sze, *Physics of Semiconductor Devices, 2nd Edition*, Wiley-Interscience, New York **1981**, pp. 79–81.
[18] P. Peumans, A. Yakimov, S. R. Forrest, *J. Appl. Phys.* **2003**, *93*, 3693.
[19] A. Nollau, M. Pfeiffer, T. Fritz, K. Leo, *J. Appl. Phys.* **2000**, *87*, 4340.
[20] M. Chikamatsu, T. Taima, Y. Yoshida, K. Saito, K. Yase, *Appl. Phys. Lett.* **2004**, *84*, 127.
[21] K. Walzer, B. Maennig, M. Pfeiffer, K. Leo, *Chem. Rev.* **2007**, *107*, 1233.
[22] V. D. Mihailetchi, P. W. M. Blom, J. C. Hummelen, M. T. Rispens, *J. Appl. Phys.* **2003**, *94*, 6849.
[23] A. G. Werner, F. Li, K. Harada, M. Pfeiffer, T. Fritz, K. Leo, *Appl. Phys. Lett.* **2003**, *83*, 4495.
[24] C. K. Chan, E. G. Kim, J.-L. Brédas, A. Kahn, *Adv. Funct. Mater.* **2006**, *16*, 831.
[25] P. Peumans, S. Uchida, S. R. Forrest, *Nature* **2003**, *425*, 158.
[26] M. M. Mandoc, W. Veurman, J. Sweelssen, M. M. Koetse, P. W. M. Blom, *Appl. Phys. Lett.* **2007**. *91*, 073 518.
[27] G. Li, V. Shrotriya, J. Huang, Y. Yao, T. Moriarty, K. Emery, Y. Yang, *Nat. Mater.* **2005**, *4*, 864.
[28] S. Uchida, J. Xue, B. P. Rand, S. R. Forrest, *Appl. Phys. Lett.* **2004**, *84*, 4218.